SCIENTIFIC REPORTS

OPEN

Icosahedra clustering and short range order in Ni-Nb-Zr amorphous membranes

S. Sarker[1], D. Isheim[2], G. King[3], Q. An[1], D. Chandra[1], S. I. Morozov[4], K. Page[5], J. N. Wermer[3], D. N. Seidman[2] & M. Dolan[6]

Crystalline Pd/Pd-Ag membranes are widely used for hydrogen separation from CO_2 and other gases in power generation applications. To substitute these high cost noble metal alloy membranes, the Ni-Nb-Zr amorphous alloys are being developed that exhibit relatively high permeability of hydrogen between 200–400 °C. Atom probe tomography (APT) experiments performed on these ribbons revealed nm-scale Nb-rich and Zr-rich regions (clusters) embedded in a ternary matrix, indicating phase separation within the Ni-Nb-Zr amorphous alloy. Density functional theory (DFT) simulations have predicted that these clusters are composed of icosahedral coordination polyhedra. The interatomic distances and correlation lengths of the short range order of these alloys were determined by neutron total scattering which match well with our DFT based molecular dynamics (DFT-MD) simulations.

Ni-based amorphous alloys have been developed to replace crystalline Pd/Pd-23Ag (23% Ag) noble metal alloy membranes which are commercially available for hydrogen separation from CO_2 and other gases in power generation applications. Hara *et al.*[1] proposed using amorphous alloy membranes of $Ni_{64}Zr_{36}$ for separating hydrogen from CO_2. Since then many permeation studies were performed to understand permeation behavior of Ni-based amorphous alloys; these are discussed in a review paper[2]. In spite of the lack of long range order, these amorphous alloys show high hydrogen permeability, very good electrical transport properties, and under certain conditions show superconductivity[2,3].

In addition, metallic glasses have outstanding mechanical properties such as extreme strength and hardness, excellent formability in the supercooled liquid region, large elastic strain limit, and high wear and corrosion resistance compared with crystalline counterpart due to a lack of crystal defects and grain boundaries discussed in the literatures[4–7]. Ni based metallic glass showed 6.6% super elastic stain limit[8]. These metallic glasses possess promising applications for biomedical materials[4], light-weight structural materials[7], coating purposes[7] and magnetic core inductor[9], however, due to their brittleness, they are not widely used for commercial applications.

Therefore, it is very important to understand the nature of internal atomic arrangement of these metallic glasses. Several studies have been performed[10–12] in the past decade to understand the atomic arrangement of $(Ni_{0.60}Nb_{0.40})_{70}Zr_{30}$ glassy ribbons. There are reports of icosahedral structure formation inside the ribbon[3,11,13], although fundamental understanding of the cluster formation, structural configuration, internal atomic arrangement and chemical homogeneity in this amorphous ribbon are still lacking. Also, phase separation (chemical heterogeneity) in Ni-Nb-Zr amorphous membranes, without prior annealing to crystallization and cluster effects on glass formability, mechanical, electrical and dynamic properties have not been reported earlier to the best of our knowledge.

To address these issues we performed a combination of atom probe tomography (APT) and neutron scattering (HIPD) experiments coupled with the density functional theory (DFT) based molecular dynamics (MD) simulations on the membrane alloy ribbons of $(Ni_{0.60}Nb_{0.40})_{70}Zr_{30}$. The APT experiments were performed in order

[1]Departments of Chemical and Materials Engineering, University of Nevada, Reno, Nevada, 89557, USA. [2]Department of Materials Science and Engineering, Center for Atom Probe Tomography, Northwestern University, 2220 Campus Dr., Evanston, IL, 60028, USA. [3]Materials Science and Technology Division, Los Alamos National Laboratory, Los Alamos, NM, 87545, USA. [4]Department of Computer Simulation and Nanotechnology, South Ural State University, Chelyabinsk, 454080, Russia. [5]Chemical and Engineering Materials Division, Oak Ridge National Laboratory, Oak Ridge, TN, 37831, USA. [6]CSIRO, Division of Energy Technology, Kenmore, QLD 4069, Australia. Correspondence and requests for materials should be addressed to S.S. (email: suchismita13994@gmail.com) or Q.A. (email: qia@unr.edu) or D.C. (email: dchandra@unr.edu)
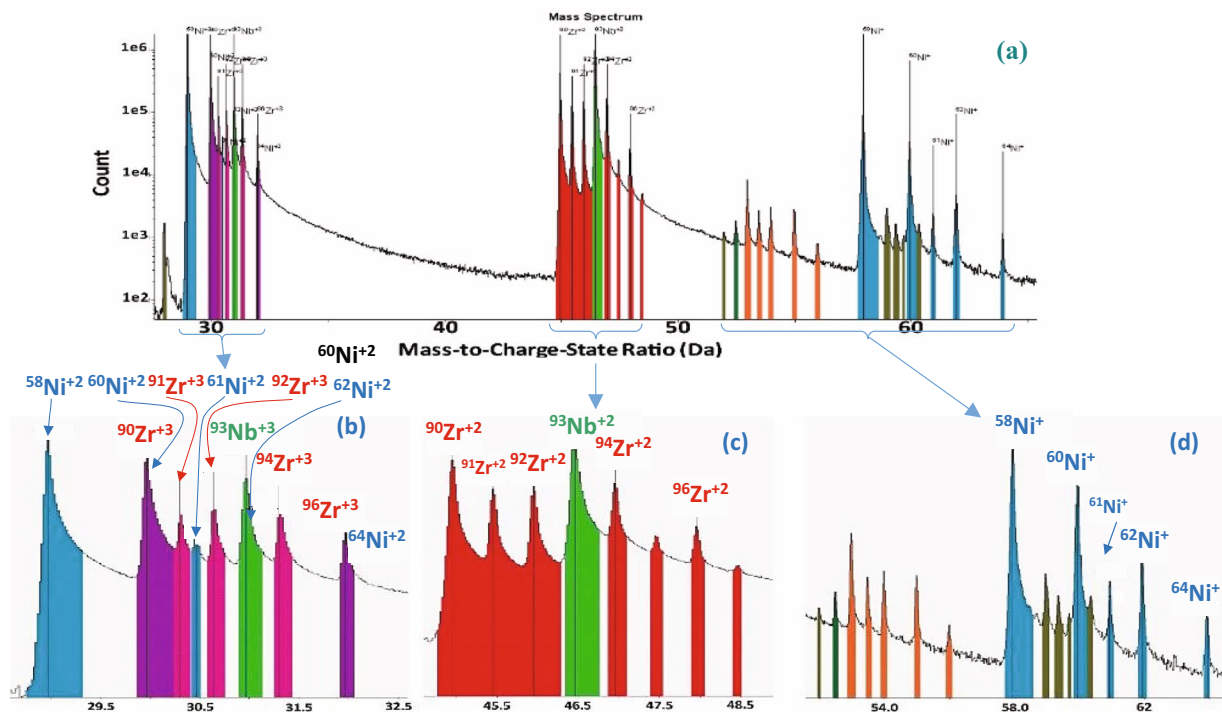
Figure 1. (**a**) The overall mass spectrum binned in 0.02 amu in the mass reange 27–66 amu for the area shown in figure, (**b**) expanded region of the spectra in 0.02 bins 27–66 amu, (**c**) expanded region of the spectra in 0.02 bins 43.5–50 amu, (**d**) expanded region of the spectra in 0.02 bins 50–66 amu.

to understand the chemical heterogeneity and local chemical composition of these alloys and to determine the possible existence of clusters and their average sizes and compositions. These APT data allowed us to reconstruct three dimensional structures revealing Nb-rich and Zr-rich clusters embedded in a ternary matrix whose compositions deviated from the nominal overall composition of the membrane. Here we used phase separation to represent the emergence of the Nb-rich and Zr-rich clusters embedded in the glass matrix (chemical heterogeneity). Next, we performed a neutron total scattering experiment that gave interatomic distances between all types of atom-atom pairs. Finally, the DFT-MD simulations provided detailed local cluster information of Nb-rich and Zr-rich clusters in the Ni-rich matrix. In addition, the radial distribution functions derived from the DFT-MD simulations gave the interatomic distance between atom pairs corroborated very well with those of the experimentally determined values. In this study, we present the local atomic order of the $(Ni_{0.60}Nb_{0.40})_{70}Zr_{30}$ glassy alloy membrane ribbon and discuss cluster formation obtained from the APT experiments and interatomic distances between atoms measured by neutron scattering experiments and DFT simulations.

Results and Discussion

Atom Probe Tomography.   Atom Probe Tomography (APT) was performed on the needle shaped specimen of $(Ni_{0.60}Nb_{0.40})_{70}Zr_{30}$ obtained from the thin alloy membrane. The alloying elements Ni, Nb, Zr and their respective isotopes are detected by time-of-flight mass spectrometry, following field-evaporation of the atoms activated by the laser pulses. The mass spectra show the isotopic peaks for Ni^+, Ni^{2+}, Zr^{2+}. Zr^{3+}, Nb^{2+}, and Nb^{3+} in the range ~28 to 65 mass-to-charge-state ratio (in "amu" units). For clarity, we expanded the three sections where the peaks are located as shown in Fig. 1. The expanded range of 28.5–32.5 amu shows the peaks of Ni^{2+} (isotopes 58, 60, 61, 62, and 64) and Zr^{3+} (isotopes 90, 91, 92, 94, and 96) and Nb^{3+} (isotope 93) in Fig. 1(b). There are isobaric overlaps between the peaks for $^{60}Ni^{2+}$ and $^{90}Zr^{3+}$, $^{64}Ni^{2+}$ and $^{96}Zr^{3+}$, and $^{62}Ni^{2+}$ and $^{93}Nb^{3+}$. In the range of 44.5–49 amu, all isotopic peaks of Zr^{2+}(90, 91, 92, 94, and 96) and one peak for $^{93}Nb^{2+}$ are observed in Fig. 1(c). The peaks of Ni^+(58, 60, 61, 62, and 64), and other Hf, Ta, O (complex molecular ions $(ZrO)^{2+}$) and C $(NbC)^{2+}$ impurities are observed in the mass range 52–64.5 amu, Fig. 1(d). For convenience, a complete list of the isotope mass numbers, atomic mass, and natural isotope abundances and the typical charge states for the elements Ni, Nb and Zr are shown in Table 1. The isobaric overlaps are corrected to obtain the overall compositions with a deconvolution calculation based on the respective isotopic abundances. While this correction can be done for a collection of ions with sufficient counting statistic, it cannot be applied for determining the chemical identity of individual ions, this limits the capability for atomically resolving individual coordination polyhedra, in addition to the 50% detection efficiency limit mentioned above. A three dimensional APT reconstruction of the glassy alloy $(Ni_{0.60}Nb_{0.40})_{70}Zr_{30}$ shows the distribution of Ni, Nb, and Zr atoms in a 113 nm × 109 nm × 99 nm volume in Fig. 2(a). Figure 2(b–d) show the distribution of individual elements Ni (blue), Nb (Green) and Zr (Red) atoms in this reconstruction volume. The nominal average composition of the amorphous matrix of this ribbon is Ni = 42 at.%, Nb = 28 at.% and Zr = 30 at.%. Even though the atomic distribution appears to be fairly uniform

Phase Name	Abbreviation	Elemental Concentration (at.%)					
		Ni	Statistical error	Nb	Statistical error	Zr	Statistical error
Overall Nominal	$Ni_{42}Nb_{28}Zr_{30}$	42	—	28	—	30	—
Overall measured by APT	$Ni_{42}Nb_{26}Zr_{32}$	41.97	±0.07	26.05	±0.03	31.98	±0.07
Phase I (Nb-rich cluster)	$Ni_{32}Nb_{46}Zr_{22}$	31.8	±0.6	46.5	±0.4	21.7	±0.7
Phase II (Zr-rich cluster)	$Ni_{39}Nb_{18}Zr_{44}$	38.6	±0.8	17.9	±0.3	43.45	±1.1

Table 1. Composition of Phase I (Nb-rich cluster), Phase II (Zr-rich cluster), and overall composition of the alloy from the atom probe tomography studies.

NiNbZr 113 × 109 × 99 nm³
20112484 atoms
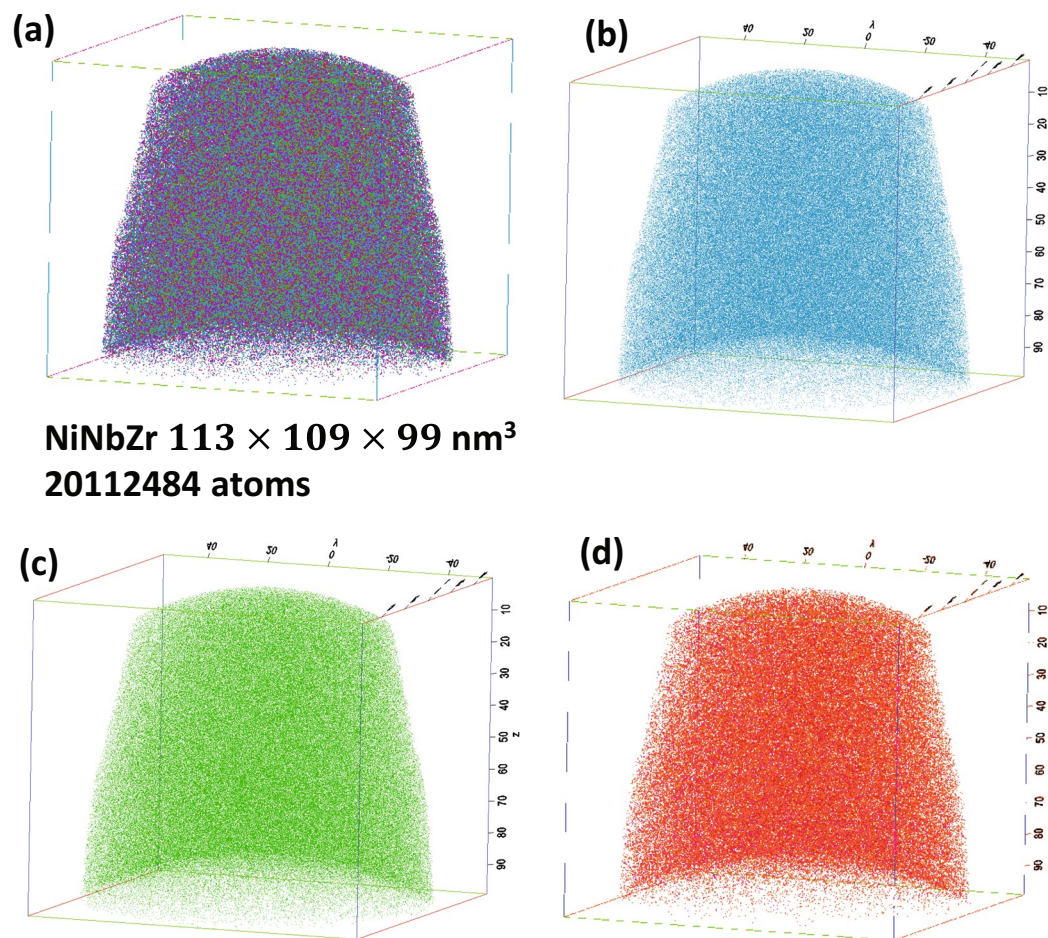
Figure 2. Atom probe 3D reconstruction of a portion of the $(Ni_{60}Nb_{40})_{70}Zr_{30}$ needle shaped specimen showing (**a**) ~20.1 million atoms of Ni, Nb and Zr, and other small impurities in a section 113 × 109 × 99 nm³ volume, (**b**) Ni atoms (isolated), (**c**) Nb atoms (isolated), and Zr atoms (isolated).

to the eye, the local composition needs to be characterized with respect to potential (i) local nanometer-scale compositional variations related to decomposition of multiple amorphous phases, and (ii) we seek information about the atomic arrangement, short range order (SRO), and polyhedra.

The presence of compositional variations or inhomogeneities is shown in the Fig. 3. The graph shows the distributions of concentrations for Zr and Nb determined from small blocks containing N = 600 atoms. The comparison with the binomial distribution, dashed lines, representing a uniform atomic distribution, reveals that both the measured distributions are significantly broader than the uniform distribution with significant tails to higher Zr concentrations above 29 at.% Zr and higher Nb concentration above 34 at.%. The significance of the concentration tails and broadening relative to a uniform alloy was confirmed with a chi-square test. The arrows in Fig. 3 delineate compositions, 29 at.% Zr or 34 at.% Nb, above which the majority of blocks with concentrations above these limits are non-random. We use these concentration thresholds in the following for isolating the Zr or Nb-rich regions, their spatial distribution, and perform a detailed on positional analysis.

We first revisit the spatial distribution of Zr, Nb, and Ni in a small volume slice of 113 × 5 × 99 nm³ selected from the center of the original volume of 113 × 109 × 99 nm³, as shown by dotted lines Fig. 4(a). The atomic
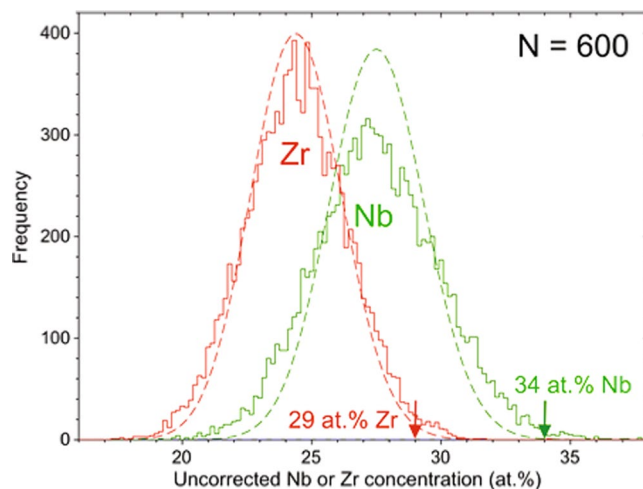
Figure 3. Concentration frequency distribution analysis of a subvolume of the APT reconstruction of the $(Ni_{0.60}Nb_{0.40})_{70}Zr_{30}$ melt-spun ribbon.

reconstruction and 34 at.% Nb isoconcentration surfaces revealed inhomogeneous amorphous structure with Nb-rich clusters embedded in a Ni-rich matrix. Sections in the *y* and *z* directions can be seen in Fig. 4(b) and (c). We will first discuss the detection of the Nb-rich clusters in the matrix. The matrix has 28 at.% Nb, but varying the concentration greater or less than 28 at.% we observe Nb-rich clusters of different composition than the nominal ones (Fig. 4(d)); other atoms $113 \times 109 \times 99$ nm^3 of 34% Nb, that shows the same clusters as seen in Fig. 4(d), but superimposed with lower concentration Nb-atoms. The position of the clusters remains the same when these 34% Nb atoms are superimposed with the Ni (Fig. 4(f)), and Zr (Fig. 4(g)) atoms. We designate this Nb-rich cluster as *Phase I*. In a similar manner we determined Zr rich (*Phase II*) in the matrix by using a 29 at.% Zr isoconcentration surface, Fig. 5(a). These results clearly suggest phase separation even at room temperature in the amorphous alloy $(Ni_{0.60}Nb_{0.40})_{70}Zr_{30}$ ribbon with separate Nb and Zr-rich clusters, respectively. In Fig. 4(e) we show Nb atoms above and below the threshold iso-concentration. The distributions of isolated Zr-rich clusters (in red color) in a small volume are shown in Fig. 5(a); the dots representing other atoms are left out for clarity. The spatial distribution of both Nb- and Zr rich regions in the $(Ni_{0.60}Nb_{0.40})_{70}Zr_{30}$ ribbon are shown in Fig. 5(b). The average composition of the ribbon as measured by the APT is Ni = 41.89 at.%, Nb = 26.14 at.%, Zr = 31.97 at.% which is very close to the nominal alloy composition of Ni = 42 at.%, Nb = 28 at.%, Zr = 30 at.% of the melt spun ribbon. Table 2 shows the composition of Nb and Zr enriched cluster which are distinctly different than the nominal composition of the alloy. We estimated the cluster size of Zr-rich region as ~2–3 nm, and ~4–5 nm in the Nb-rich region from Fig. 5.

So far, we have identified the presence of Zr- and Nb- rich clusters in the amorphous matrix, but the detailed atomic structure of these clusters and actual short range order remain to be determined. We established characteristic nearest neighbor (NN) distances of Ni-Ni, Nb-Nb, and Zr-Zr in the ribbon by APT, using the algorithm implemented in the IVAS3.6.12 software package, similar to the approach described by Shariq *et al.*[13,14] for measuring the nearest neighbor distance in ternary amorphous alloys by APT. This approach assumes that the limited detection efficiency and spatial resolution in APT results in a broadening of the NN distance distribution, but not in a shift of the most likely NN distance, preserving the non-random information related to local short-range order in a coordination polyhedron, so that the most frequent distance in the distribution can be identified with the actual next-neighbor pair distance, in our case the Ni-Ni, Nb-Nb, and Zr-Zr next neighbor pair distances. This approach can be justified if, on average, at least one next neighbor of each constituent element is preserved in the APT reconstruction. Given a 50% detection efficiency of the APT detector, and 12–14 next neighbor atoms in a typical coordination polyhedron, 6-7 next neighbors of each atom are preserved, on average, in the APT reconstruction. Since at least one atom of each elemental species is needed for resolving the atomic pairings of the coordination polyhedron, a minimum average atomic concentration of 14–17 at.% is required which is the case for the amorphous alloys studied by Shariq *et al.*[13,14]. In our case, however, the isobaric overlaps between some of the elements and charge states in the mass spectrum, see Fig. 1 and Table 1, further reduce the amount of usable information. Specifically, to unambiguously identify Ni and Zr, only the isotopes 58 for Ni and the isotopes 91, 92, and 94 for Zr can be used, representing 68.077% of Ni and 45.75% of Zr, see Table 1. We neglect the small contribution of $^{62}Ni^{++}$ to the large peak for $^{93}Nb^{3+}$ at 31 amu. Given the atomic elemental concentrations listed in Table 2, this results in an isotopic concentration for ^{58}Ni of 28.6 at%, and only 14.6% for Zr, which is close to the very limit of where the assumption of having at least one next neighbor atom present in the reconstruction, on average, breaks down, which will result in an increased error of the measurement. The loss of structural information relating to the short-range order for lower elemental or isotopic concentrations will cause a shift of the peak in the next-neighbor distribution, in addition to the broadening mentioned above, as discussed by Philippe *et al.*[15] for the very different case of randomly distributed solute atoms in a dilute solution. For the sake of comparison, we determined the next-neighbor distances for the Ni-Ni, Nb-Nb, and Zr-Zr atom pairs in the amorphous
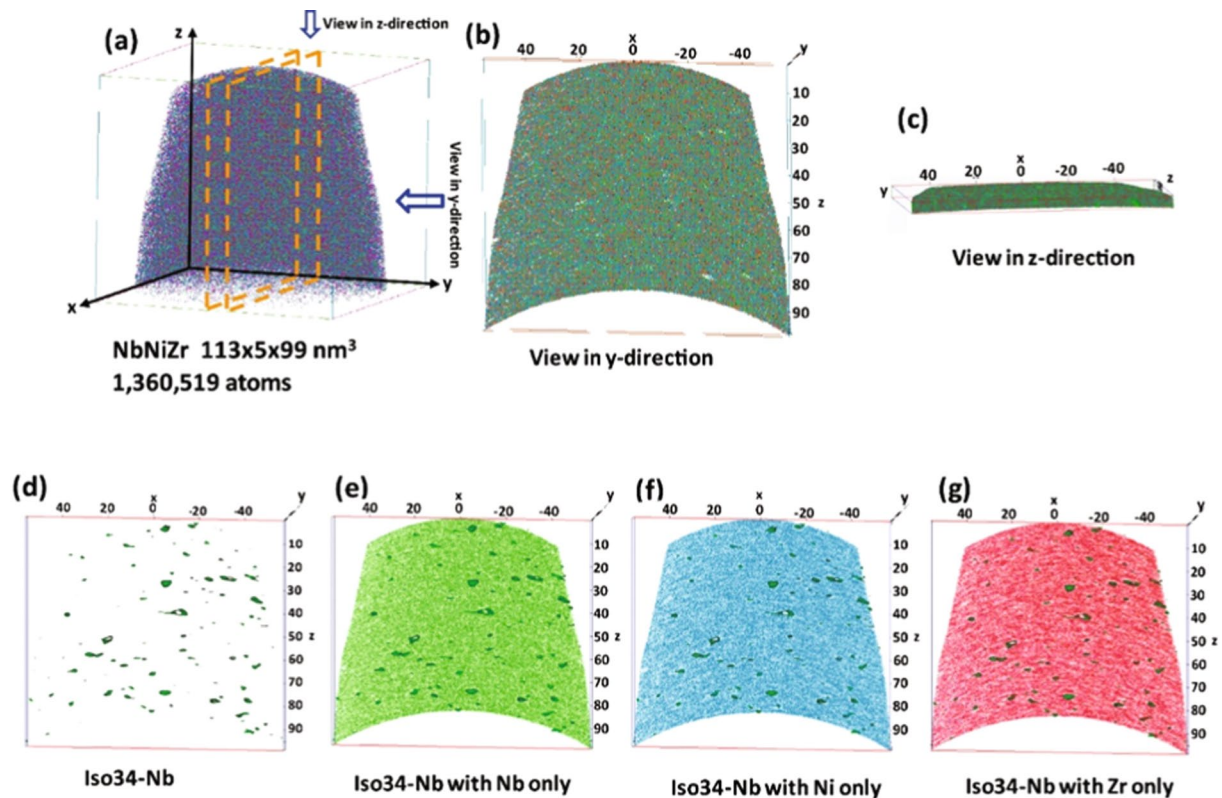
Figure 4. (**a**) Atom probe 3D reconstruction of a portion of the $(Ni_{0.60}Nb_{0.40})_{70}Zr_{30}$ sample in a cropped volume of $113 \times 5 \times 99$ nm^3 showing all the Ni, Nb, and Zr atoms, (**b**) view in y-direction, (**c**) view in z-direction, (**d**) Iso34-Nb, (**e**) Iso34-Nb with Nb atoms (isolated), (**f**) Iso34-Nb with Ni atoms (isolated), and (**g**) Iso34-Nb with Zr atoms (isolated).

$(Ni_{0.60}Nb_{0.40})_{70}Zr_{30}$ alloy with the approach outlined by Shariq et al.[13,14], using the most likely distance in the next-neighbor distribution, and the resulting distances are given in Table 3.

In the literature, Kelton et al.[16] reported experimental demonstration of Frank hypothesis in $Ti_{39.5}Zr_{39.5}Ni_{21}$ alloy in undercooled liquids local structure that contained a significant degree of short-range order (SRO) icosahedra, with no long-range periodicity. Many others reported metallic glass systems have a significant degree of order within the amorphous matrix[15,16]. Icosahedral short range order has been found in various metallic glasses and its fraction has been used as a characteristic indicator of the formation of metallic glasses[17,18].

There are examples of Zr-based amorphous alloys that showed phase separation and nanoscale icosahedral clusters formation in a single amorphous phase by APT close to glass transition temperature[19]. The DFT-MD simulation reveals a similar type of icosahedral structure appearing in our ribbon at room temperature[3,11,12,19]. In another paper, Hono et al.[20] obtained three dimensional APT data in which they observed clustering of Cu just prior to primary crystallization. Shariq and Mattern's APT study[21] revealed phase separation in $Ni_{66}Nb_{17}Y_{17}$ alloy, where the Y-rich phase is depleted of Nb and vice-versa. They also found two interconnected amorphous phases similar to what we observed in our Ni-Nb-Zr alloy. There are reports of amorphous thin films in the immiscible copper–niobium system in which phase separation was observed even at low temperatures, 200 °C[22]. Mattern et al.[23] studied as-quenched $Cu_{46}Zr_{47-x}Al_7Gd_x$ metallic glasses and found that the cluster formation was dependent on the Gd content in the alloy; this formation is favorable at higher temperatures due to pre-crystallization nucleation and growth. All the above mentioned literature and our APT data suggested that phase separation might be a common behavior in the majority of the amorphous materials. Our ribbon is stable for several weeks during the permeation experiments, suggesting that the phase separation occurred during quenching in the melt spinning process.

In 2009, Oji et al.[11,12] reported icosahedral structure in $(Ni_{0.60}Nb_{0.40})_{70}Zr_{30}$ and $(Ni_{0.60}Nb_{0.40})_{60}Zr_{40}$ alloys using XAFS data and other computational models. Further studies by Fukuhara and Inoue[3] using XANES confirmed that these glassy alloys have formed icosahedra. Oji et al.[12] proposed two possible icosahedra structure models Zr_6Ni_6Nb and $Ni_5Nb_3Zr_5$ for the ternary alloys. A distorted icosahedral structure of $Ni_5Nb_3Zr_5$ type was reported for the alloy of $(Ni_{0.60}Nb_{0.40})_{60}Zr_{40}$ by molecular dynamics calculations[3,11]. In order to understand detailed local cluster structures inside these Ni-based amorphous ribbons by considering the experimental APT data, DFT-MD simulation were performed. The DFT-MD simulations cannot predict the whole experimental samples because of the limited size scale to hundreds of atoms. However, it can provide physical insight on the local heterogeneous cluster structures composed by a hundred of atoms. The DFT-MD results suggest that the amorphous structure consists of different types of icosahedra shown in the Table 3; these icosahedra consists of 12 atoms (Voronoi index (0 0 12 0)) and most of them are Ni and Nb centered. The Nb- and Zr-rich clusters in the alloys have
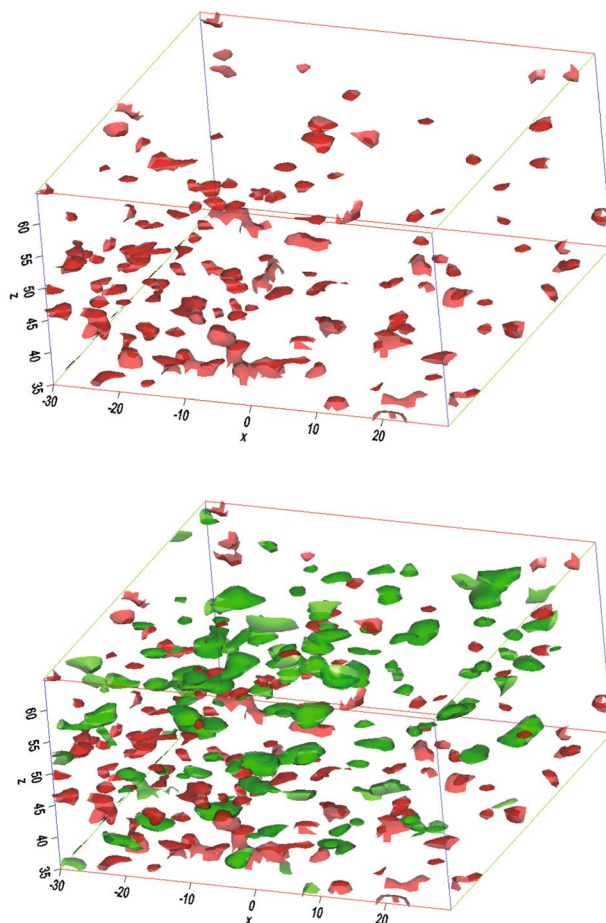
Figure 5. (**a**) Zirconium rich regions delineated by a 29 at.% isoconcentration surface (red color), (**b**) niobium rich regions (34 at.% isoconcentration surface, green color). The cluster size of niobium is comparatively bigger than the cluster size of zirconium.

Element	Ni			Zr			Nb		
	Atom-nm³	At. wt.	At. No	Atom-nm³	At. wt.	At. No	Atom-nm³	At. wt.	At. No
	91.4	**58.693**	**28**	**43.0**	**91.224**	**40**	**64.2**	**92.906**	**41**
Charge State	+	++	+++	+	++	+++	+	++	+++
Evaporator Field (V/nm)	**35**	36	65	**56**	28	35	**74**	37	45
Sr. No.	*Isotope Mass No.	Isotope (At. %)	Atomic mass (Da)	*Isotope Mass No.	Isotope (At. %)	Atomic mass (Da)	*Isotope Mass No.	Isotope (At. %)	Atomic mass (Da)
1	58*	57.935	68.077	90*	89.905	51.45	93*	92.906	100
2	60*	59.931	26.223	91*	90.906	11.22			
3	61*	60.931	1.140	92*	91.905	17.15			
4	62*	61.928	3.635	94*	93.906	17.38			
5	64*	63.928	0.926	96*	95.908	2.8			

Table 2. Stable isotopes of and field-evaporation properties of Ni, Zr, and Nb for time-of-flight mass spectrometry in atom-probe tomography (Bold indicate most probable Charged State).

Element Pair	Ni-Ni	Nb-Nb	Zr-Zr
Interatomic Next-neighbor distance measured by APT (nm)	~2.53	~2.65	~3.05

Table 3. Next-neighbor distances for Ni-Ni, Nb-Nb, and Zr-Zr pairs measured by atom-probe tomography.

Icosahedron	$Ni_{41}Nb_{59}Zr_{28}$	$Ni_{49}Nb_{23}Zr_{56}$
1	$Ni_2Nb_7Zr_3$ (Zr)	$Ni_3Nb_4Zr_5$ (Nb)
2	$Ni_4Nb_4Zr_4$ (Nb)	$Ni_2Nb_4Zr_6$ (Nb)
3	$Ni_4Nb_6Zr_2$ (Nb)	$Ni_4Nb_2Zr_6$ (Ni)
4	$Ni_2Nb_5Zr_5$ (Nb)	
5	$Ni_1Nb_7Zr_4$ (Ni)	
6	$Ni_3Nb_6Zr_3$ (Ni)	
7	$Ni_4Nb_5Zr_3$ (Ni)	
Average over icosahedra	$Ni_{16}Nb_{30}Zr_{18}$	$Ni_9Nb_{10}Zr_{17}$
Average over all	$Ni_{31}Nb_{49}Zr_{26}$	$Ni_{33}Nb_{18}Zr_{48}$

Table 4. Different icosahedra configurations for Nb-rich ($Ni_{41}Nb_{59}Zr_{28}$) and Zr-rich ($Ni_{49}Nb_{23}Zr_{56}$) with centered atom in parenthesis calculated by DFT-MD.

different icosahedral chemical formulas as expected shown in Table 4. The DFT simulation reveals the average size of single icosahedron is ~0.56 nm.

The Fig. 6 showed snapshot of (a) nominal composition ($Ni_{54}Nb_{36}Zr_{38}$), (b) Zr-rich region ($Ni_{49}Nb_{23}Zr_{56}$) and (c) Nb-rich region ($Ni_{41}Nb_{59}Zr_{28}$) where Ni, Nb and Zr atoms are represented by grey, cyan and green balls respectively. The atoms with icosahedra clusters represented by red atoms revealed that the Nb rich cluster is composed of 7 icosahedra (~3.9 nm) and Zr- rich cluster is composed of 3 icosahedra (~1.7 nm) which are similar to the experimental data shown in Fig. 5. The cluster typically observed in small region composed of hundred atoms and it is randomly arranged throughout the glass. The APT experimental and DFT-MD simulation shows that the cluster sizes in these metallic glasses between 2–5 nm as a function of different alloying additions[23]. Fujima et al.[24] reported 8 icosahedra of $Ni_5Nb_3Zr_5$ single unit in $(Ni_{0.60}Nb_{0.40})_{60}Zr_{40}$ alloy using first principle calculation; according to their calculation local icosahedra structure are stable in the amorphous phase at room temperature. Although we observed the icosahedral clusters at room temperature in DFT-MD simulations, we expected that the phase separation in experiments happens at supercooled liquid where not many icosahedral clusters are formed[18].

These interconnected icosahedra affect both structural and dynamical properties of metallic glasses[25,26]. Wen et al.[25] performed a series of MD simulations which reveal correlation of glass forming ability (GFA) and icosahedral clusters. We proposed that the Nb and Zr interconnected icosahedral clusters increase glass forming ability[27] as they lower the atomic packing and minimize the energy, thus stabilize the amorphous structure[28].

During solidification, the atoms which help to form medium range icosahedra clusters play a crucial role in formation of amorphous alloy. Yang et al.[29] study reveals these interconnected icosahedra progressively increase with decreasing temperature. The APT and DFT-MD simulation reveals tendency to form favorable Nb-rich cluster than Zr-rich cluster. These Nb-rich interconnected icosahedra cause more compact and higher density (7.94 g/cm^3) structure than Zr-rich (7.46 g/cm^3) region. Because of these interconnected Nb icosahedral clusters, it is difficult for supercooled liquid to form another metastable basin[26] which internally restrain crystallization; the system is completely amorphous even at room temperature. Fujima et al.[24] also proposed similar effect of Nb atoms on these amorphous materials.

The strength of the metallic glass increases as number of full icosahedra increase which causes more resistance to the plastic flow of the alloys[27,30]. This plastic flow can be initiated by decreasing full icosahedra of Nb and Zr-rich regions and increasing homogeneity of clusters throughout the matrix. The APT and DFT results showed Nb-rich region is composed of 7 icosahedra, thus, exhibit excellent structural and thermal stability. Non-isotherm DSC experiment also showed crystallization temperature and the thermal stability increases with an addition of Nb in Ni-ETM alloy[31].

The studies on the Ni-Nb-Zr alloy with addition of hydrogen by Fukuhara et al.[32] suggested sub-nanometersized two different icosahedra cluster configurations that an play important role in the electronic transport behavior of the alloy. Our APT study reveals these clusters are distributed throughout the matrix shown in the Fig. 4, therefore electron travelling through the two different icosahedra is comparatively easier and provides sufficient justification for coulomb oscillation, ballistic transport and superconductivity.

Dynamic heterogeneity such as β-relaxation process is also affected by nano-scale heterogeneity throughout the matrix[33]. The structural relaxation of these amorphous materials depends on the interconnected icosahedra cluster formation. The reason for the relaxation time increases may be due to larger connectivity of icosahedra clusters in Nb-rich and Zr-rich region[26]. In this $(Ni_{0.6}Nb_{0.4})_{70}Zr_{30}$ metallic glass, the β relaxation time in vacuum is 9780 seconds[34]. The dominant Nb-rich and Zr –rich interconnected full icosahedra are responsible for the dynamic slowdown of this metallic glass[27]. From potential-energy landscape perspective, due to five-fold symmetry of full icosahedra in both Nb and Zr rich regions, the metallic glass has higher configurational transition barrier, thus deep local minima, which causes increase in relaxation time.

In the permeation study, Zr is added to the base alloy $Ni_{60}Nb_{40}$ to increase the hydrogen permeation rate. It is possible that the phase separation or cluster formation is enhanced due to the addition of Zr in the Ni-Nb amorphous alloy as the empirical atomic size of zirconium ($r_{Zr} = 155$ pm) is much larger than of Ni ($r_{Ni} = 135$ pm) and Nb ($r_{Nb} = 145$ pm); the more the Zr in the Ni-Nb alloy, greater the tendency for phase separation[35]. This reason also is applicable for the dynamic slowdown of the system.
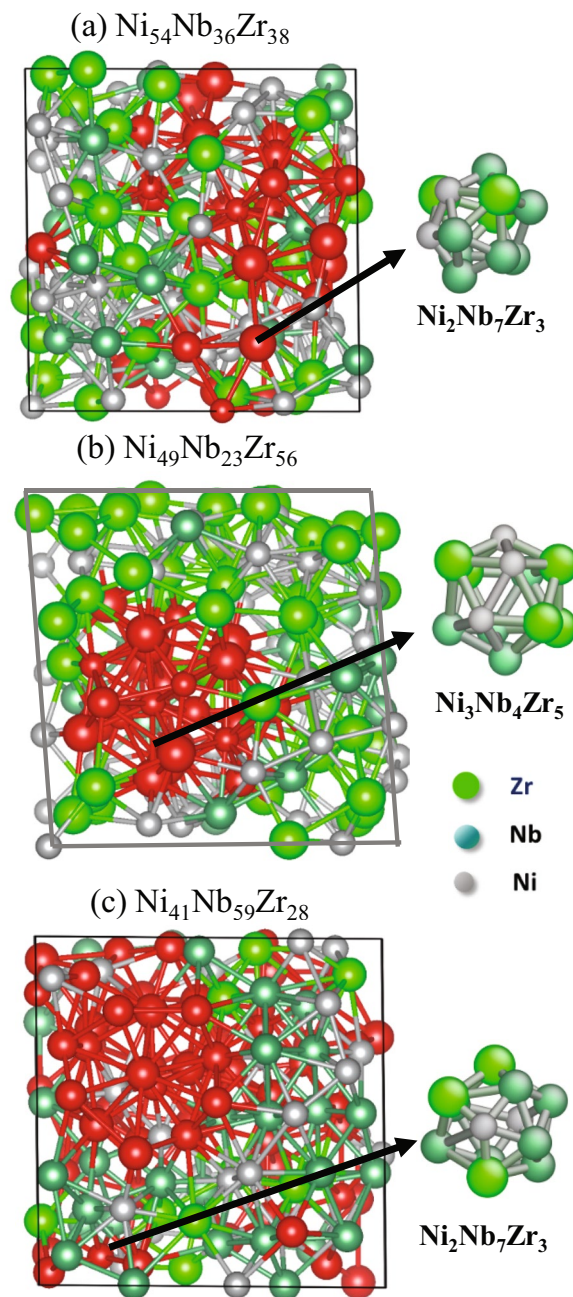
Figure 6. Snapshots of various ternary metallic glasses which are formed during the fast quenching from high temperature of 3000 K with the cooling rate of 1.08×10^{14} s^{-1}. The atoms within icosahedral clusters are represented by red balls in the periodic simulation box. The Zr, Nb and Ni atoms are represented by green, cyan and grey balls, respectively.

Neutron Total Scattering. We could not determine the interatomic distance of different pairs of atoms, such as Zr-Ni or Ni-Zr by the APT in the $(Ni_{0.60}Nb_{0.40})_{70}Zr_{30}$ alloy with better precision, due to detection efficiencies issues and the isobaric overlaps in the mass spectrum, that effectively further reduce the number of atoms that can be identified unambiguously. We turned to total neutron scattering performed at LANSCE (Los Alamos National Laboratory). The pair distribution function (PDF) data shows the number of atomic pairs separated by a distance of "r" and therefore that serves as an excellent probe of the local structure of disordered materials. The PDF of the $(Ni_{0.60}Nb_{0.40})_{70}Zr_{30}$ alloy (in Fig. 7a) showed well defined features of the short range order up to ~1.8 nm with no structural correlations at longer length scales. The first peak in the PDF plot represents the nearest neighbor atomic distances and has contributions from interatomic bond distances. This first peak has a main feature at ~0.268 nm and two high-r shoulders. The low-r feature represents bond distances involving Ni and is the most prominent feature because Ni is the most common element and has the strongest neutron scattering length. The Ni-Ni distances are expected to be the shortest, but in our case we observed them to be longer (0.240–0.270 nm) as compared to the Ni-Ni distance of only 0.248 nm in the pure metallic Ni, whereas the average
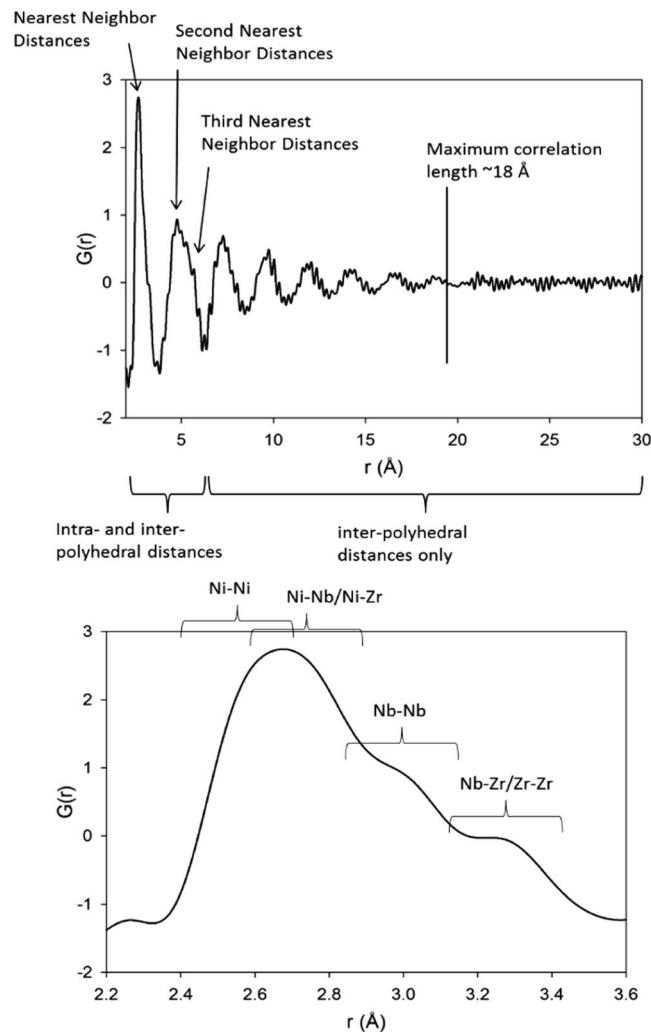
Figure 7. (**a**) Pair distribution function of $(Ni_{0.60}Nb_{0.40})_{70}Zr_{30}$ showing features up to ~1.8 nm. (**b**) Details of overlapped regions of the first nearest neighbors distances of Ni-Ni, Ni-Nb/Ni-Zr, Nb-Nb, and Nb-Zr/Zr-Zr.

Ni-Ni distance is probably a few hundredths of an Å shorter than the 0.268 peak, there are clearly no atom-atom pairs with average distances as short as 0.248 nm. We did not find any feature at or around 0.248 nm, concluding that there are no regions in this material where Ni is coordinated mostly or entirely by Ni in this ternary alloy. Thus it is expected that the matrix of this ribbon is Ni rich with Nb and Zr atoms. We propose that the Ni-rich matrix with significant number of Nb and Zr atoms randomly distributed embeds the Nb- and Zr rich clusters. All Ni atoms appear to be bonded to significant numbers of Nb or Zr atoms, which slightly elongates the Ni-Ni distances relative to pure Ni. The higher-r part of the main feature can be expected to originate from Ni-Nb and Ni-Zr distances, which are on average slightly longer than 0.268 nm. The first high-r shoulder, is centered at ~0.295 nm, and can be expected to be primarily from Nb-Nb distances. The second shoulder at ~0.324 nm can be assigned to Nb-Zr and Zr-Zr distances.

The second peak (Fig. 7a) in the PDF represents distances from the second and third nearest neighbor distances. At higher r values there are 5 more features in the PDF representing larger distances. These peaks are all spaced between 0.22–0.25 nm, suggesting a regular pattern in the way the polyhedra are arranged relative to each other. At longer length scales the atomic positions are no longer correlated. Figure 7(b) shows expanded view of the first peak.

We also obtained interatomic distances from radial distribution function (RDF) optimizing the structure for nominal composition ($Ni_{54}Nb_{36}Zr_{38}$), Zr-rich region ($Ni_{49}Nb_{23}Zr_{56}$) and Nb-rich region ($Ni_{41}Nb_{59}Zr_{28}$) compositions from the DFT-MD simulations, as showed in the Fig. 8. The nominal composition data match with neutron total scattering experimental values. It is interesting to observe that in Nb and Zr rich region the peaks shifted on the right side, concluding Ni atom bonded with more number of Nb and Zr than the nominal composition. In the Nb-rich region ($Ni_{41}Nb_{59}Zr_{28}$), second peak of Nb-Nb distances are more prominent than other two compositions as expected. The data represented here in the Table 5 is only first atomic shell which is less than 0.360 nm observed from both experimental and simulated values. Due to smaller system consideration, the long-range order is not calculated here.
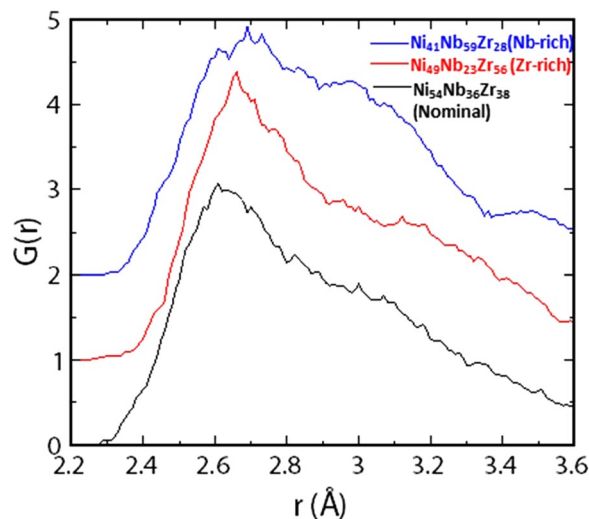
Figure 8. Radial distribution function (RDF) optimizing the structure for nominal composition ($Ni_{54}Nb_{36}Zr_{38}$), Zr-rich region ($Ni_{49}Nb_{23}Zr_{56}$) and Nb-rich region ($Ni_{41}Nb_{59}Zr_{28}$) by black, red and blue color respectively.

Element Pair	Ni-Ni	Nb-Nb	Zr-Zr	Ni-Nb	Ni-Zr	Nb-Zr
$Ni_{42}Nb_{28}Zr_{30}$ (HIPD)	~0.240–0.270	~0.295	~0.324	Slightly larger than 0.268	Slightly larger than 0.268	~0.324
$Ni_{54}Nb_{36}Zr_{38}$ (DFT –MD)	~0.262	~0.296	~0.325			
$Ni_{49}Nb_{23}Zr_{56}$ (DFT –MD)	~0.265	−0.295	~0.300–0.320			
$Ni_{41}Nb_{59}Zr_{28}$ (DFT –MD)	~0.270	~0.3	~0.340			

Table 5. The interatomic distances from Neutron Scattering and DFT-MD simulation, note that the Ni-Nb and Ni-Zr distances could not be measured accurately.

Several studies have been done in past few decades in amorphous $(Ni_{0.60}Nb_{0.40})_{70}Zr_{30}$ as well as Ni-based amorphous ribbon by x-ray diffraction in order to understand interatomic distances between atoms. The summary of the data obtained from EXAFS and XRD-RDF studies are shown in Table 6[36–46]. All the data of nearest neighbor found in the literature study are x-ray data and no reports of neutron studies are available, to best of our knowledge.

The advantage of PDF over XAFS is that later is limited to the first 1–3 coordination spheres, whereas we can access much longer interatomic distances with the PDF. The amorphous structure of $(Ni_{0.60}Nb_{0.40})_{70}Zr_{30}$ has order up to ~1.8 nanometer, but is completely disordered when viewed at longer length scales. The combination of APT, PDF and DFT-MD simulations comprehensively suggest that there are large clusters with 2–5 nm in diameter, but there is not necessarily structural coherence across the entire length of the cluster.

The cluster formation with in the amorphous material affects permeation property significantly. In general, the permeation depends on both solubility and diffusivity of the material. According to Yamuara's et al.[10] study, the solubility Ni-Zr alloy increases with the addition of Nb in the system due to change in local atomic structure. In this study of $(Ni_{0.6}Nb_{0.4})_{70}Zr_{30}$ metallic glass, Nb interconnected icosahedra cluster region appears with Zr clusters, which helps in hydrogen solubility. Fukuhara et al.[32] suggested that at lower hydrogen concentration, the hydrogen atom localizes to a site between Ni atoms that belong to different icosahedra. However, if the hydrogen content is high, hydrogen atom goes inside tetrahedral sites of distorted Zr and Nb and enlarges the icosahedra. There are several experimental and computational studies[36,37] reveal volume expansion of the alloy due to hydrogenation. The APT and DFT-MD studies show Ni-based alloys have Nb- and Zr- rich interconnected icosahedra clusters throughout the matrix. Hydrogen insertion causes increase in the cluster size due to enlargement of these icosahedra that creates path for hydrogen to pass through the membrane. It will be interesting to observe how the cluster size affects the permeation property of these Ni-Nb-Zr alloy membranes. These studies are in progress

Conclusions

Cluster formation within the matrix of Ni-rich amorphous alloy is shown unambiguously by atom probe tomography and DFT-MD simulation. Specifically, a Nb-rich phase of $Ni_{32}Nb_{46}Zr_{22}$ (cluster size ~4-5 nm), and a Zr-rich phase of $Ni_{39}Nb_{18}Zr_{44}$ (cluster size ~2–3 nm) are embedded in the Ni-rich ternary $Ni_{42}Nb_{28}Zr_{30}$ amorphous alloy matrix. The DFT-MD simulation reveals that the Nb-rich phase composed of 7 icosahedra and Zr-rich phase composed of 3 icosahedra. This study reveals Nb-rich interconnected full icosahedra restrain long range crystallization and increases stability of the metallic glass. The HIPD PDF data show that the short range order is indeed present, and extends up to ~1.8 nm. This means that there is some order beyond the length scale of a single

References	Year	Alloy	Ni-Ni r (nm)	Ni-Zr r (nm)	Zr-Ni r (nm)	Zr-Zr r (nm)	Nb-Nb r (nm)	Ni-Nb r (nm)	Nb-Zr r (nm)	Nb-Ni r (nm)	Ni-Zb r (nm)
Frahm et al.[36]	1984	$Ni_{24.1}Zr_{75.9}$	—	0.262	0.262	0.317	—	—	—	—	—
Frahm et al.[36]	1984	$Ni_{33.3}Zr_{66.7}$	—	0.262	0.262	0.318	—	—	—	—	—
Frahm et al.[36]	1984	$Ni_{36.5}Zr_{63.5}$	—	0.262	0.262	0.32	—	—	—	—	—
Lee et al.[37]	1984	$Ni_{35}Zr_{65}$	0.266	0.269	0.269	0.315	—	—	—	—	—
Lee et al.[37]	1985	$Ni_{35}Zr_{65}$	0.266	0.269	0.269	0.315	—	—	—	—	—
Frahm et al.[38]	1989	DSC $Ni_{36.5}Zr_{63.5}$	—	0.263	0.263	0.321	—	—	—	—	—
Lima et al.[39]	1988	$Ni_{25}Zr_{75}$	—	0.276	0.276	3.23	—	—	—	—	—
Paul et al.[40]	1990	$Ni_{24.1}Zr_{75.9}$	—	0.27	0.27	0.316	—	—	—	—	—
Paul et al.[40]	1990	$Ni_{33.3}Zr_{66.7}$	—	0.27	0.27	0.316	—	—	—	—	—
Paul et al.[40]	1990	$Ni_{36.5}Zr_{63.5}$	—	0.27	0.27	0.316	—	—	—	—	—
Paul et al.[40]	1990	DSC $Ni_{36.5}Zr_{63.5}$	—	0.27	0.27	0.324	—	—	—	—	—
Babanov et al.[41]	1995	$Ni_{67}Zr_{33}$	0.249	0.272	—	—	—	—	—	—	—
Lima et al.[42]	2003	a-$NiZr_2$	0.267	0.267	0.267	0.321	—	—	—	—	—
Yamuara et al.[10]	2005	$Ni_{60}Nb_{40}$	0.247	—	—	—	0.294	0.266	—	0.266	—
Yamuara et al.[10]	2005	$(Ni_{0.6}Nb_{0.4})_{70}Zr_{30}$	0.25	0.266	0.266	0.32	0.292	0.268	0.311	0.268	0.311
Sakurai et al.[43]	2005	$(Ni_{0.6}Nb_{0.4})_{70}Zr_{30}$		0.263		0.316	—	—	—	—	—
Yamuara et al.[10]	2005	$(Ni_{0.6}Nb_{0.4})_{50}Zr_{50}$	0.25	0.266	0.266	0.32	0.292	0.269	0.311	0.269	0.311
Sakurai et al.[43]	2005	$(Ni_{0.6}Nb_{0.4})_{50}Zr_{50}$	—	0.264		0.316	—	—	—	—	—
Saida et al.[44]	2007	$Ni_{30}Zr_{70}$	0.248	—	0.27	0.319	—	—	—	—	—
Oji et al.[12]	2009	$(Ni_{0.6}Nb_{0.4})_{70}Zr_{30}$	—	—	0.263	0.324			0.324	0.255	—
Oji et al.[12]	2009	$(Ni_{0.6}Nb_{0.4})_{60}Zr_{40}$	—	—	0.263	0.325	—		0.325	0.254	—
Tian et al.[45]	2012	$Ni_{62.5}Nb_{37.5}$	2.48	—	—	—	3.05	2.63	—	5.5	—
Yang et al.[46]	2013	$Ni_{60}Nb_{40}$	0.273	—	—	—	0.282	0.28	—	—	—
Yang et al.[46]	2013	$Ni_{61}Nb_{39}$	0.273	—	—	—	0.282	0.279	—	—	—
Yang et al.[46]	2013	$Ni_{62}Nb_{38}$	0.273	—	—	—	0.281	0.279	—	—	—
Yang et al.[46]	2013	$Ni_{63}Nb_{37}$	0.272	—	—	—	0.282	0.278	—	—	—
Yang et al.[46]	2013	$Ni_{64}Nb_{36}$	0.273	—	—	—	0.281	0.279	—	—	—

Table 6. The summary of nearest neighbor distance measurement from previous studies.

icosahedral unit but there is generally no structural order across the entire length of a cluster. The interatomic distances calculated from experiments and DFT-MD simulations agree very well, even though the cooling rate in simulations is much higher than experiments. In conclusion, these studies shed light on probable hydrogen permeation mechanisms, structural and dynamic properties of amorphous membranes.

Methods

High purity nickel (35.1 wt.%), niobium (33.3 wt.%) and zirconium (31.6 wt.%) powder particles were mixed and arc-melted to produce alloy buttons of $Ni_{42}Nb_{28}Zr_{30}$ at the DOE AMES Laboratory in Iowa. The fast-quenched ribbon, usually designated as, $(Ni_{0.60}Nb_{0.40})_{70}Zr_{30}$, was fabricated by a melt-spinning under argon atmosphere at CSIRO laboratory, Brisbane, Australia. The cooling rate for fabrication of this ternary ribbon was ~10^6 K/s. X-ray diffraction analysis performed on the ribbon (~50 μm thick) confirmed the amorphous nature of ribbon.

Atom Probe Tomography (APT). A focused-ion beam (FIB) instrument is used to prepare needle shaped specimens for atom probe tomography (APT). Sections of ~30 μm long lift-out volume are extracted from the fast-quenched surface of a melt spun ribbon and mounted on the top of standard APT microtip array tips, and ion milled to form a needle with a sharp tip whose radius of curvature is ~30–50 nm. The samples were then transferred to a Cameca LEAP 4000X Si for APT analysis. APT can achieve a spatial resolution of better than 0.3 nm in three dimensions, and high analytical sensitivity of ~1 atomic parts per million (at.ppm) in reconstructed sample volumes of typically 106 nm3 (100 nm × 100 nm × 100 nm). The detection efficiency of the LEAP 4000X Si is approximately 50%. In spite of these limitations, APT is the best probe available for studying local compositions in materials on a sub-nm scale in three dimensions. For the APT studies, a pulsed laser beam is utilized, with a wavelength of 355 nm (ultraviolet) and 20 pJ pulse energies to activate atom-by-atom field evaporation, with a pulse repetition frequency of 500 kHz and a specimen stage temperature of 30 K. More details on the APT method can found in refs[47–49].

Neutron Total Scattering. The ribbon of $(Ni_{0.60}Nb_{0.40})_{70}Zr_{30}$ was loaded in the HIPD instrument at the Lujan Neutron Scattering Center of Los Alamos National Laboratory and neutron total scattering data was collected. The pair distribution function, G(r), was generated from S(Q) using a Q_{max} of 25 Å^{-1} with the program PDFgetN; details can be found in the ref.[50].

Quantum molecular dynamics simulation.   The atomic structures and interatomic distances in $(Ni_{0.60}Nb_{0.40})_{70}Zr_{30}$ alloy membrane are calculated by DFT and DFT-based molecular dynamics (DFT-MD) simulations. The DFT-MD simulations (or *ab initio* molecular dynamics simulations) use interatomic forces calculated from quantum mechanics. All these calculations are performed using VASP (The Vienna Ab initio Simulation Package) with plane wave basis set[51,52]. The Perdew-Burke-Ernzerhof (PBE) Functional is applied for the generalized gradient approximation (GGA) exchange-correlation functional. In addition, the full potential projector augmented-wave (PAW) method was adopted for the core-valence interaction. To optimize the local structure of amorphous alloy, the energy cutoff for plane wave expansions was set to 600 eV. For supercell calculations, reciprocal space was sampled using the Γ-centered Monkhorst-Pack scheme with gamma point only. For geometric optimization, the force convergence criterion is considered as 10^{-3} eV/A° and electronic self-consistent field (SCF) convergence is 10^{-6} eV.

The DFT-MD simulation steps are discussed below. We started with the composition $Ni_{54}Nb_{36}Zr_{38}$ in which 128 atoms were randomly placed in the supercell with the cell length of 12.86 Å along three directions. This leads to a density of 7.79 g/cm^3, and the other two systems of Zr-rich composition $Ni_{49}Nb_{23}Zr_{56}$ and Nb-rich composition $Ni_{41}Nb_{59}Zr_{28}$ are also constructed with the initial density of 7.46 and 7.94 g/cm^3, respectively. The systems were first heated from room temperature to 3000 K within 2 ps and then equilibrated at 3000 K for 5 ps using NVT ensemble (constant volume, constant temperature and constant number of atoms). Finally the systems are quenched from 3000 K to room temperature over the period of 25 ps with a fixed volume. This leads to a very fast quench rate of 1.08×10^{14} K/s. The time step is set to 2 fs in the DFT-MD simulations. The convergence criterion is set to a 1×10^{-4} eV energy difference for solving the electronic wave function in DFT-MD simulations. After we obtained the amorphous structures in DFT-MD simulations, we performed geometry relaxation using DFT to relax the internal stress. Then we performed the structural analyses such as RDF and Voronoi analysis[53] on these relaxed structures. The radial distribution function (RDF) describes how density varies as a function of distance from a reference particle. It is a very useful tool to distinguish the structures between crystal and amorphous materials. The RDF only reveals the average structure information. To characterize the topological short range order, we use the Voronoi tessellation analysis. Here the indices (n3, n4, n5, n6) represent the number of i-edge faces of the polyhedron where the sum of ni gives the coordination number (CN) of the center atom.

References

1. Hara, S. *et al.* An amorphous alloy membrane without noble metals for gaseous hydrogen separation. *Journal of Membrane Science* **164**, 289–294 (2000).
2. Sarker, S. *et al.* Developments in the Ni–Nb–Zr amorphous alloy membranes. *Applied Physics A*, 122–168 (2016).
3. Fukuhara, M. & Inoue, A. Electric resistivity and thermoelectricity of Ni–Nb–Zr and Ni–Nb–Zr–H glassy alloys. *Physica B*, 3630–3622 (2010).
4. Chen, M. A brief overview of bulk metallic glasses. *NPG Asia Mater.* **3**, 82–90 (2011).
5. Sha, Z. D. *et al.* Metallic glass-based chiral nanolattice: Light weight, auxeticity, and superior mechanical properties. *Materials Today* **20**(10), 569–576 (2017).
6. Miller, M. *et al.* Bulk Metallic Glasses, Springer Science, NY, USA, ISBN 978-0-387-48920-9 (2008).
7. Liu, Z. Q. & Zhang, Z. F. Mechanical properties of structural amorphous steels: Intrinsic correlations, conflicts, and optimizing strategies. *Journal of Applied Physics*, **114**, 243519-1-14, 116 (2013).
8. Jiang, Q. K. *et al.* Super elastic strain limit in metallic glass films. *Scientific Report* **2**(852), 1–6 (2012).
9. Inoue, A. *et al.* Development and application of Fe-based soft magnetic bulk metallic glassy inductors. *Journal of Alloys and Compounds* **731**, 1303–1309 (2018).
10. Yamaura, S. I. *et al.* Hydrogen permeation and structural features of melt-spun Ni–Nb–Zr amorphous alloys. *Acta Materialia* **53**, 3703–3711 (2005).
11. Oji, H. *et al.* Local atomic structure around Ni, Nb, and Zr atoms in Ni-Nb-Zr-H glassy alloys. *Journal of Physics: Conference Series* **190**, 012075 (2009).
12. Oji, H. *et al.* Local atomic structure around Ni, Nb, and Zr atoms in Ni–Nb–Zr–H glassy alloys studied by x-ray absorption fine structure method. *Journal of Applied Physics* **105**, 113527 (2010).
13. Shariq, A., Al-Kassab, T. & Kirchheim, R. Studying nearest neighbor correlations by atom probe tomography (APT) in metallic glasses as exemplified for $Fe_{40}Ni_{40}B_{20}$ glassy ribbons. *Journal of Alloys and Compounds* **512**, 270–277 (2012).
14. Shariq, A. *et al.* Exploring the next neighborhood relationship in amorphous alloys utilizing atom probe tomography. *Ultramicroscopy* **107**, 773–780 (2007).
15. Philippe, T. *et al.* Clustering and nearest neighbor distances in atom-probe tomography. *Ultramicroscopy* **109**, 1304–1309 (2009).
16. Kelton, K. F. *et al.* First X-Ray scattering studies on electrostatically levitated metallic liquids: demonstrated influence of local icosahedral order on the nucleation barrier. *Physical Review Letters* **90**, 195504 (2003).
17. Sha, Z. D. *et al.* Statistical composition-structure-property correlation and glass-forming ability based on the full icosahedra in Cu–Zr metallic glasses. *Applied Physics Letter*, **96**, 061903-1,3 (2010).
18. An, Q. *et al.* Predicted Optimum Composition for the Glass-Forming Ability of Bulk Amorphous Alloys: Application to Cu–Zr–Al. *Journal of Physical Chemistry Letter* **3**(21), 3143–314812 (2012).
19. Martin, I. *et al.* Nano-crystallization of $Zr_{41.2}Ti_{13.8}Cu_{12.5}Ni_{10.0}Be_{22.5}$ metallic glass. *Acta Materialia* **52**, 4427–4435 (2004).
20. Hono, K. *et al.* Cu clustering and Si partitioning in the early crystallization stage of an $Fe_{73.5}Si_{13.5}B_9Nb_3Cu_1$ amorphous alloy. *Acta Materialia* **47**, 997–1006 (1999).
21. Shariq, A. & Mattern, N. A study of phase separated $Ni_{66}Nb_{17}Y_{17}$ metallic glass using atom probe tomography. *Ultramicroscopy* **111**, 1370–1374 (2011).
22. Puthucode, A. *et al.* De-vitrification of nanoscale phase-separated amorphous thin films in the immiscible copper–niobium system. *Philosophical Magazine* **94**, 1622–1641 (2003).
23. Mattern, N. *et al.* Phase separation in $Cu_{46}Zr_{47-x}Al_7Gd_x$ metallic glasses. *Journal of Alloys and Compounds* **509S**, S23–S26 (2011).
24. Fujima, N. *et al.* M. Local structures and structural phase change in Ni-Zr-Nb glassy alloys composed of $Ni_5Zr_5Nb_3$ icosahedral clusters. *Journal of Applied Physics* **114**, 063501 (2013).
25. Wen, D. D. *et al.* Correlation of the heredity of icosahedral clusters with the glass forming ability of rapidly solidified Cu_xZr_{100-x} alloys. *Journal of Non-Crystalline Solids* **427**, 199–207 (2015).
26. Wu, Z. W. *et al.* Correlation between structural relaxation and connectivity of icosahedral clusters in CuZr metallic glass-forming liquids. *Physical Review B* **88**, 054202 (2013).

27. Cheng, Y. Q. *et al*. Local order influences initiation of plastic flow in metallic glass: Effects of alloy composition and sample cooling history. *Acta Materialia* **56**, 5263–5275 (2008).
28. Sheng, H. W. *et al*. Atomic packing and short-to-medium range order in metallic glasses. *Nature* **439**, 419–425 (2006).
29. Yang, M. H. *et al*. Atomic-scale simulation to study the dynamical properties and local structure of Cu–Zr and Ni–Zr metallic glass-forming alloys. *Physical Chemistry Chemical Physics* **18**, 7169–7183 (2016).
30. Lee, M. *et al*. Networked interpenetrating connections of icosahedra: Effects on shear transformations in metallic glass. *Acta Materialia* **59**, 159–170 (2011).
31. Dolan, M. *et al*. Ni-based amorphous alloy membranes for hydrogen separation at 400 °C. *Journal of Membrane Science* **326**, 549–555 (2009).
32. Fukuhara, M. *et al*. Effect of hydrogen and cluster morphology on the electronic behavior of Ni-Nb-Zr-H glassy alloys with sub-nanometer-sized icosahedral $Zr_5Ni_5Nb_3$ clusters. *The European Physical Journal D* **67**, 40 (2013).
33. Feng, S. D. *et al*. The role of configurational disorder on plastic and dynamic deformation in $Cu_{64}Zr_{36}$ metallic glasses: A molecular dynamics analysis. *Scientific Reports* **7**, 40969, https://doi.org/10.1038/srep40969 (2017).
34. Sarker, S. Atom Dynamics of Amorphous Materials by X-Ray Photon Correlation Spectroscopy (XPCS) & Neutron Spectroscopy, Ph.d. diss, University of Nevada, Reno, ProQuest Dissertations Publishing, 2017 (10619898), ISBN: 9780355263503; (http://hdl.handle.net/11714/2064).
35. Zhua, Z. W. *et al*. Synthesis and properties of bulk metallic glasses in the ternary Ni–Nb–Zr alloy system. *Materials Science and Engineering A* **492**, 221–229 (2008).
36. Frahm, R. *et al*. EXAFS studies of the local order in amorphous and crystalline nickel-zirconium alloys: II. Structure of the amorphous alloys. *Journal of Physics F* **14**, 1333–1346 (1984).
37. Lee, A., Etherington, G. & Wagner, C. N. J. Partial structure functions of amorphous $Ni_{35}Zr_{65}$. *Journal of Non-Crystalline Solids* **61-62**, 349–354 (1984).
38. Frahm, R., Haensel, R. & Rabe, P. EXAFS studies of intermediate crystallisation steps of amorphous Ni-Zr alloys. *Journal of Physics: Condensed. Matter* **l**, 1521–1525 (1989).
39. Lima, deJ. C., Tonnerre, J. M. & Raoux, D. Anomalous wide angle X-ray scattering of amorphous Ni_2Zr alloy. *Journal of Non-Crystalline Solids* **106**, 38–41 (1988).
40. Paul, F. & Frahm, R. Short range order in amorphous Ni-Zr alloys. *Physical Review B* **42**, 10945–10949 (1990).
41. Babanov, Y. A., Schvetsov, V. R. & Sidorenko, A. F. Atomic structure of binary amorphous alloys by combined EXAFS and X-ray scattering. *Physica B* **208-209**, 375–376 (1995).
42. Lima, deJ. C. *et al*. Structural study of an amorphous $NiZr_2$ alloy by anomalous wide-angle x-ray scattering and reverse Monte Carlo simulations. *Physical Review B* **67**, 094210 (2003).
43. Sakurai, M., Yamura, S., Wakoh, K., Matsubara, E. & Inoue, A. Structure and hydrogen permeation of Ni-Nb-Zr amorphous alloy. *Journal of Metastable and Nano-crystalline Materials* **24-25**, 551–554 (2005).
44. Saida, J. *et al*. Correlation between local structure and stability of supercooled liquid state in Zr-based metallic glasses. *Materials Science and Engineering A* **449–451**, 90–94 (2007).
45. Tian, H. *et al*. Ab initio molecular dynamics simulation of binary $Ni_{62.5}Nb_{37.5}$ bulk metallic glass: validation of the cluster-plus-glue-atom model. *Journal of Material Science* **47**, 7628–7634 (2012).
46. Yang, L., Meng, X. & Guo, G. Structural origin of the pinpoint-composition effect on the glass-forming ability in the NiNb alloy system. *Journal of Materials Research* **28**, 3170–3176 (2013).
47. Kelly, T. F. *et al*. First data from a commercial local electrode atom probe (LEAP). *Microscopy and Microanalysis* **10**, 373–383 (2004).
48. Miller, M. K., Cerezo, A., Hetherington, M. G. & Smith, G. D. W. Atom Probe Field IonMicroscopy: Oxford Univ. Press, and Miller MK. 2000. Atom Probe Tomography: Analysis at the Atomic Level. (New York: Kluwer Acad./Plenum, 1996).
49. Larson, D. J., Prosa, T. J., Ulfig, R. M., Geiser, B. P. & Kelly T. F. *Local Electrode Atom Probe Tomography: A User's Guide*. (New York: Springer, 2013)
50. Peterson, P. F., Gutmann, M., Proffen, T. & Billinge, S. J. L. PDFgetN: a user-friendly program to extract the total scattering structure factor and the pair distribution function from neutron powder diffraction data. *Journal of Applied Crystallography* **33**, 1192 (2000).
51. Kresse, G. & Furthmuller, J. Efficient iterative schemes for *ab initio* total-energy calculations using a plane-wave basis set. *Physical Review B* **54**, 11169–11186 (1996).
52. Kresse, G. & Joubert, D. From ultrasoft pseudopotentials to the projector augmented-wave method. *Physical Review B* **59**, 1758–1775 (1999).
53. An, Q. *et al*. How the toughness in metallic glasses depends on topological and chemical heterogeneity. *Proceedings of the National Academy of Sciences* **113**(26), 7053–7058 (2016).

Acknowledgements

Author Contributions

S.S., D.C., and Q.A. designed this project. S.S., D.C., and Q.A. collect the data and constructed the manuscript. D.I. and D.N.S. performed APT experiments and analyses the data. S.I.M. and Q.A. performed the DFT simulations. S.S., G.K. and J.N.W. performed Neutron Scattering experiments. K.P. and M.D. contributed to the scientific discussion and manuscript presentation. All authors reviewed the manuscript and agreed to submit the paper.

Additional Information

Publisher's note: Springer Nature remains neutral with regard to jurisdictional claims in published maps and institutional affiliations.